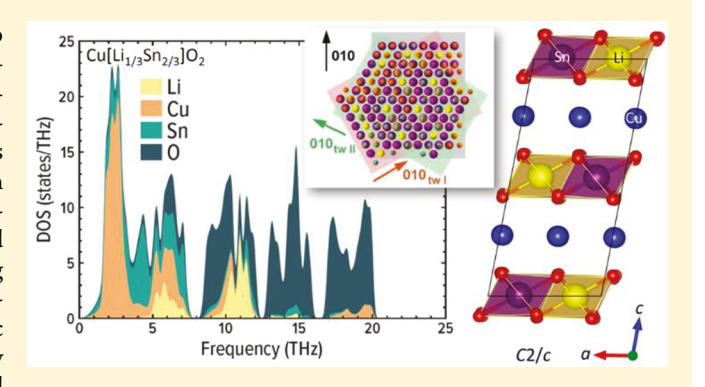
pubs.acs.org/IC

# Crystal Chemistry and Phonon Heat Capacity in Quaternary Honeycomb Delafossites: Cu[Li<sub>1/3</sub>Sn<sub>2/3</sub>]O<sub>2</sub> and Cu[Na<sub>1/3</sub>Sn<sub>2/3</sub>]O<sub>2</sub>

Mykola Abramchuk,<sup>†</sup> Oleg I. Lebedev,<sup>‡</sup> Olle Hellman,<sup>†,§</sup> Faranak Bahrami,<sup>†</sup> Natalia E. Mordvinova,<sup>‡</sup> Jason W. Krizan,<sup>†</sup> Kenneth R. Metz,<sup>||</sup> David Broido,<sup>†</sup> and Fazel Tafti\*,<sup>†</sup>

Supporting Information

ABSTRACT: This work presents an integrated approach to study the crystal chemistry and phonon heat capacity of complex layered oxides. Two quaternary delafossites are synthesized from ternary parent compounds and copper monohalides via a topochemical exchange reaction that preserves the honeycomb ordering of the parent structures. For each compound, Rietveld refinement of the powder X-ray diffraction patterns is examined in both monoclinic C2/c and rhombohedral R3m space groups. Honeycomb ordering occurs only in the monoclinic space group. Bragg peaks associated with honeycomb ordering acquire an asymmetric broadening known as the Warren line shape that is commonly observed in layered structures with stacking disorder. Detailed



TEM analysis confirms honeycomb ordering within each layer in both title compounds and establishes a twinning between the adjacent layers instead of the more conventional shifting or skipping stacking faults. The structural model is then used to calculate phonon dispersions and heat capacity from first principles. In both compounds, the calculated heat capacity accurately describes the experimental data. The integrated approach presented here offers a platform to carefully analyze the phonon heat capacity in complex oxides where the crystal structure can produce magnetic frustration. Isolating phonon contribution from total heat capacity is a necessary and challenging step toward a quantitative study of spin liquid materials with exotic magnetic excitations such as spinons and Majorana fermions. A quantitative understanding of phonon density of states based on crystal chemistry as presented here also paves the way toward higher efficiency thermoelectric materials.

# **■ INTRODUCTION**

The delafossite structural family comprises a myriad of layered oxides with the basic formula ABO2 where A can be either an alkali or a noble metal (Cu, Ag, Pt, Pd), and B can be almost any transition metal.1 A combination of mixed valency, site preference, and layered structure in delafossites gives rise to a wide range of applicable functions including ionic conductivity, photocatalytic activity, thermoelectric performance, and magnetic frustration.<sup>2-7</sup> Analyzing the crystal chemistry of delafossites is challenging for two reasons: (a) the weak bonding between the layers may result in stacking disorders such as skipping, shifting, or twinning of the layers, and (b) the hexagonal packing of different atomic species within each layer may produce honeycomb ordering and change the space group. Depending on the stacking sequence (bilayer or trilayer) and the in-plane ordering (hexagonal or honeycomb), four common space groups are proposed for the ternary and quaternary delafossites including hexagonal  $P6_3/mmc$ , rhombohedral  $R\overline{3}m$ , and monoclinic C2/c or C2/m. This work is a first attempt to

connect the rich crystal chemistry of delafossites to their lattice dynamics and phonon dispersions. Such efforts will strongly impact our understanding of the thermoelectric and magnetic properties of layered oxides. For example, spin-1/2 honeycomb delafossites are one of the few candidate materials for the Kitaev spin liquid phase where the magnetic ordering is suppressed due to a competition between the Kitaev and Heisenberg interactions on a planar honeycomb geometry. 7-10 A crucial step in the study of spin liquids is to subtract the lattice (phonons) contribution from the total heat capacity and isolate the contribution from magnetic excitations, namely, magnons or spinons. At present, this analysis is performed either by fabricating a nonmagnetic version of the magnetic delafossite, which is not always possible, 11 or by estimating a T3-Debye background, which is not always reliable. To address this issue, we target the synthesis of two new nonmagnetic quaternary delafossites

Received: July 5, 2018 Published: October 1, 2018



<sup>&</sup>lt;sup>†</sup>Department of Physics, Boston College, Chestnut Hill, Massachusetts 02467, United States

<sup>\*</sup>Laboratorie CRISMAT, ENSICAEN-CNRS, UMR6508, 14050 Caen, France

<sup>§</sup>Division of Engineering and Applied Science, California Institute of Technology, Pasadena, California 91125, United States

Department of Chemistry, Boston College, Chestnut Hill, Massachusetts 02467, United States

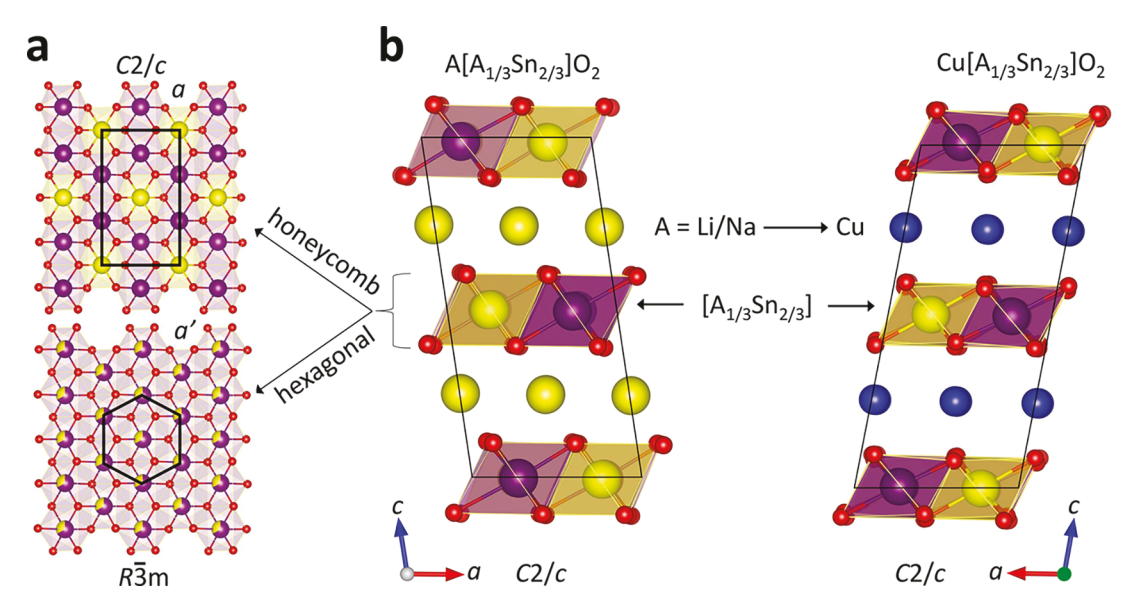


Figure 1. (a) Honeycomb ordering in the monoclinic C2/c space group (top) compared to the plain hexagonal packing in the rhombohedral  $R\overline{3}m$  space group (bottom). Note the change of unit cell from the hexagonal (bottom) with lattice parameter a to the base-centered monoclinic (top) with lattice parameters  $a' = \sqrt{3} a$ , b' = 3a. (b) Topochemical relation between the parent compounds  $A[A_{1/3}Sn_{2/3}]O_2$  with A = Li/Na and the metastable phases  $Cu[A_{1/3}Sn_{2/3}]O_2$  made by cation-exchange reaction. The honeycomb layers stay unchanged, but the interlayer alkali (yellow) are replaced by copper atoms (blue). Note the oxygen coordinates are different between the two structures. In the parent structure (left), the interlayer alkali are surrounded by six oxygens (three above and three below), forming an octahedral coordination. In the copper-exchanged phase (right), the adjacent layers are slightly shifted so the oxygens appear directly above and below each Cu atom, forming a linear (dumbbell) coordination.

and present a first comprehensive study of the relation between the crystal chemistry, phonon dispersions, and lattice heat capacity. The remarkable agreement between theoretically computed and experimentally measured heat capacity in these complex oxides implies that phonon dispersions and density of states can be reliably computed with the methods presented here. Therefore, the magnon/spinon contribution can reliably be isolated from the measured total heat capacity of the magnetic delafossites. Before presenting the results, we provide a brief introduction to the layered structure of ternary delafossites with or without honeycomb ordering and the topochemistry of quaternary delafossites.

Each layer in a ternary delafossite (ABO<sub>2</sub>) is made of edgesharing BO<sub>6</sub> octahedra, and the adjacent layers are separated by the A atoms. The stacking sequence of layers determines whether the unit cell is a hexagonal bilayer (P63/mmc, CuFeO2type) or a rhombohedral trilayer ( $R\overline{3}m$ , AgFeO<sub>2</sub>-type). Honeycomb ordering occurs when extra A atoms substitute for 1/3 of the B atoms in each layer  $(B \rightarrow [A_{1/3}B_{2/3}])$  as illustrated in Figure 1a. The ratio B/A = 2/1 is constrained by the multiplicities of the Wyckoff sites occupied by B and A atoms within each layer. As a result, honeycomb delafossites have a formula  $A[A_{1/3}B_{2/3}]O_2$  or equivalently  $A_2BO_3$  ( $A_3[AB_2]O_6$ ) instead of ABO<sub>2</sub>. Figure 1a shows how honeycomb ordering changes the unit cell from a primitive hexagonal to a base-centered monoclinic (C2/c or C2/m). If the in-plane unit cell parameter of the hexagonal system is a, the unit cell parameters of the monoclinic system must be  $a' = \sqrt{3} a$  and b' = 3a. A quaternary delafossite A'[A<sub>1/3</sub>B<sub>2/3</sub>]O<sub>2</sub> can be synthesized by exchanging the interlayer A atoms with different A' atoms via a topotactic exchange reaction:

$$A[A_{1/3}B_{2/3}]O_2 + A'X \rightarrow A'[A_{1/3}B_{2/3}]O_2 + AX$$
 (1)

Typically, A is an alkali (A = Li, Na), A' is a noble metal (A' = Cu, Ag, Pt, Pd), and X is a halogen. The topotactic reaction is

driven by the reactivity of the halide reagent (A'X) and the stability of the alkali salt product (AX). Both quaternary delafossites  $\text{Cu}[\text{Li}_{1/3}\text{Sn}_{2/3}]\text{O}_2$  and  $\text{Cu}[\text{Na}_{1/3}\text{Sn}_{2/3}]\text{O}_2$  in this work are synthesized according to eq 1 with A = Li/Na, A' = Cu, and X = Cl/I (see Figure 1b). In the remainder of this article, we analyze the structural chemistry of the title compounds by crystallographic refinements and electron microscopy. Details of the honeycomb ordering and stacking disorder are scrutinized by a combination of imaging techniques. The resulting structural solutions are then used to compute the phonon dispersions and the heat capacity. Finally, a comparison is made between the theoretically computed and the experimentally measured heat capacity.

# **■ EXPERIMENTAL SECTION**

Materials Synthesis. The precursors, Li[Li<sub>1/3</sub>Sn<sub>2/3</sub>]O<sub>2</sub> and Na[Na<sub>1/3</sub>Sn<sub>2/3</sub>]O<sub>2</sub>, were synthesized by a solid state reaction in air. To synthesize Li[Li<sub>1/3</sub>Sn<sub>2/3</sub>]O<sub>2</sub>, a stoichiometric mixture of Li<sub>2</sub>CO<sub>3</sub> (Alfa Aesar 99.998%, dried at 120 °C for 24 h) and tin(IV) oxide SnO2 (Alfa Aesar, 99.9%) was thoroughly ground under an inert atmosphere in an agate mortar and placed into a covered alumina crucible. The crucible was heated at 5 °C/min to 740 °C, kept at 740 °C for 20 h, then cooled at 10 °C/min to 300 °C, and quenched into the antechamber of an argon glovebox with O<sub>2</sub> and H<sub>2</sub>O content < 0.1 ppm. To synthesize Na[Na<sub>1/3</sub>Sn<sub>2/3</sub>]O<sub>2</sub>, a finely ground stoichiometric mixture of Na<sub>2</sub>CO<sub>3</sub> (Alfa Aesar, 99.5%, dried at 120 °C for 24 h) and SnO<sub>2</sub> was calcined in a similar way at 800 °C for 12 h before cooling to 600 °C and quenching.<sup>2</sup> Samples were successively annealed for 20 h in 50 °C steps up to 1000 °C to reduce the amount of stacking disorder in the crystal structure (see Figure S1 in the Supporting Information). For both compounds, 5-10% excess Li<sub>2</sub>CO<sub>3</sub> or Na<sub>2</sub>CO<sub>3</sub> was added at each annealing step to compensate for the volatility of lithium and sodium at high temperatures. The topotactic reactions were performed according to eq 1 by mixing Li[Li<sub>1/3</sub>Sn<sub>2/3</sub>]O<sub>2</sub> and CuCl (Alfa Aesar, 99.999%) or Na[Na<sub>1/3</sub>Sn<sub>2/3</sub>]-O<sub>2</sub> and CuI (Alfa Aesar, 99.998%) in the mole ratio 1:2 (i.e., with 100% excess copper(I) halides). The mixtures with total mass of 300 mg were pressed into 6 mm diameter pellets and placed in covered

alumina crucibles inside evacuated quartz tubes. The tubes were heated at 1  $^{\circ}$ C/min to 400  $^{\circ}$ C (Li-containing phase) or to 380  $^{\circ}$ C (Na-containing phase), annealed at those temperatures for 24 h, and then cooled to room temperature at the same rate. In order to remove the excess of CuCl (CuI) and LiCl (NaI), all samples were ground and washed five times with ammonium hydroxide (NH<sub>4</sub>OH, Alfa Aesar, 28%) and twice with deionized water. After the aqueous leaching, samples were dried at room temperature under vacuum for 1 h and subsequently at 120  $^{\circ}$ C in air for 1 h. Once dried, the samples were found to be stable in air with no changes of color, physical appearance, or powder X-ray diffraction pattern after 24 h at ambient conditions.

**X-ray diffraction.** Powder X-ray diffraction (PXRD) data were collected in reflection mode (Bragg—Brentano geometry) using a Bruker D8 ECO instrument equipped with a copper X-ray source (Cu  $K\alpha$ ), a nickel filter to absorb the  $K\beta$  radiation, and with two 2.5° Soller slits after the source and before the LYNXEYE XE 1D energy-dispersive detector. Rietveld refinement on the PXRD patterns was performed using the FullProf suite. <sup>13</sup> Peak shapes were modeled with the Thompson—Cox—Hastings pseudo-Voigt profile convoluted with axial divergence asymmetry.

**Thermal Analysis.** Differential scanning calorimetry (DSC) was performed with a NETZSCH STA 449 F1 instrument to determine the decomposition temperature of  $\text{Cu}[\text{Li}_{1/3}\text{Sn}_{2/3}]O_2$  and  $\text{Cu}[\text{Na}_{1/3}\text{Sn}_{2/3}]O_2$ . Samples were placed inside covered alumina pans and heated to 1200 °C at 5 °C/min under a 20 mL/min flow of argon.

**Optical Spectroscopy.** Inductively coupled plasma optical emission spectroscopy (ICP-OES) was performed using the Agilent model 5100 VDV spectrometer operating in axial mode. The quantitative analysis was done using standards with nine different concentrations of each metal. The Na and Cu standards were made by dissolving NaCl and CuSO<sub>4</sub>·5H<sub>2</sub>O in a mixture of HCl/HNO<sub>3</sub>. The Li and Sn standards were made from the Inorganic Ventures 1000 ppm standard solutions diluted in the mixture of HCl/HNO<sub>3</sub>. The experimental uncertainties were calculated by a propagation of error analysis using linear direct calibration plots. <sup>14</sup> Diffuse reflectance spectra (DRS) for the powder samples were collected using an Agilent Cary 7000 universal spectrometer equipped with an integrating sphere and converted from reflectance to absorbance. <sup>15</sup>

Electron Microscopy. Scanning electron microscopy (SEM) and energy-dispersive X-ray spectroscopy (EDX) were performed using Zeiss Ultra-55 and JEOL JSM 6340F field emission scanning electron microscopes (FESEM), each equipped with an EDAX detector. Transmission electron microscopy (TEM) including electron diffraction (ED), high-angle annular dark-field scanning TEM (HAADF-STEM), annular bright-field scanning TEM (ABF-STEM), and electron energy loss spectroscopy (EELS) experiments were performed using an aberration double-corrected JEM ARM200F microscope operated at 200 kV and equipped with a CENTURIO EDX detector, Orius Gatan CCD camera, and GIF Quantum spectrometer. TEM samples were prepared by grinding the materials in an agate mortar with ethanol and depositing the obtained suspension on a Ni-carbon holey grid.

**Heat Capacity Measurements.** Heat capacity measurements on pressed pellets of samples were performed using a Quantum Design PPMS Dynacool. Small rectangular pieces were broken from the pellet (m=4-5 mg) and mounted onto a sapphire micro-calorimeter platform using Apiezon N grease.

**First-Principles Calculations.** The heat capacities for  $\text{Li}[\text{Li}_{1/3}\text{Sn}_{2/3}]\text{O}_2$ ,  $\text{Na}[\text{Na}_{1/3}\text{Sn}_{2/3}]\text{O}_2$ ,  $\text{Cu}[\text{Li}_{1/3}\text{Sn}_{2/3}]\text{O}_2$ , and  $\text{Cu}[\text{Na}_{1/3}\text{Sn}_{2/3}]\text{O}_2$  were calculated from first-principles using the temperature dependent effective potential (TDEP) approach. <sup>16,17</sup> In this approach, thermally relevant atomic displacements were generated for a supercell of atoms, and the corresponding harmonic forces between atoms were calculated using density functional theory as implemented in the VASP code. <sup>18</sup> Interatomic force constants were obtained from the force—displacement relationships and used to calculate phonon modes, from which the heat capacity was then determined.

## RESULTS AND DISCUSSION

Chemical, Optical, and Spectroscopic Analyses. Title compounds were synthesized via the following topotactic cation-exchange reactions under mild conditions (380–400 °C, 24 h):

$$\label{eq:Li} {\rm Li}[{\rm Li}_{1/3}{\rm Sn}_{2/3}]{\rm O}_2 \, + \, {\rm CuCl} \, \to \, {\rm Cu}[{\rm Li}_{1/3}{\rm Sn}_{2/3}]{\rm O}_2 \, + \, {\rm LiCl} \eqno(2)$$

$$Na[Na_{1/3}Sn_{2/3}]O_2 + CuI \rightarrow Cu[Na_{1/3}Sn_{2/3}]O_2 + NaI$$
 (3)

Using mild conditions is necessary because both compounds are metastable phases with low decomposition thresholds as confirmed by a DSC analysis. Figure S2 in the Supporting Information shows decomposition of both compounds above 400 °C. The choice of CuCl/CuI in eqs 2/3 is justified by size considerations. A larger anion such as  $I^-$  (compared to  $Cl^-$ ) participates more efficiently in an exchange reaction with a larger cation such as  $Na^+$  (compared to  $Li^+$ ). Examples of failed attempts to exchange lithium stannate with CuI and sodium stannate with CuCl are provided in the Supporting Information (Figure S3).

Chemical compositions of both title compounds were determined by EDX and ICP-OES experiments (Figures S4–S6 in the Supporting Information). EDX confirmed the ratio Cu/Sn = 1.5(1), and ICP-OES confirmed the formulas Cu<sub>3.08(2)</sub>Li<sub>1.05(2)</sub>-Sn<sub>2.00(2)</sub>O<sub>6</sub> and Cu<sub>3.15(1)</sub>Na<sub>0.93(1)</sub>Sn<sub>2.00(2)</sub>O<sub>6</sub> equivalent to (Cu-[Li<sub>1/3</sub>Sn<sub>2/3</sub>]O<sub>2</sub>)  $\times$  3 and (Cu-[Na<sub>1/3</sub>Sn<sub>2/3</sub>]O<sub>2</sub>)  $\times$  3. Both compounds were found to be insulators with comparable band gaps in the visible range ( $E_{\varphi}$  = 2.2 eV). Figure 2 compares the diffuse

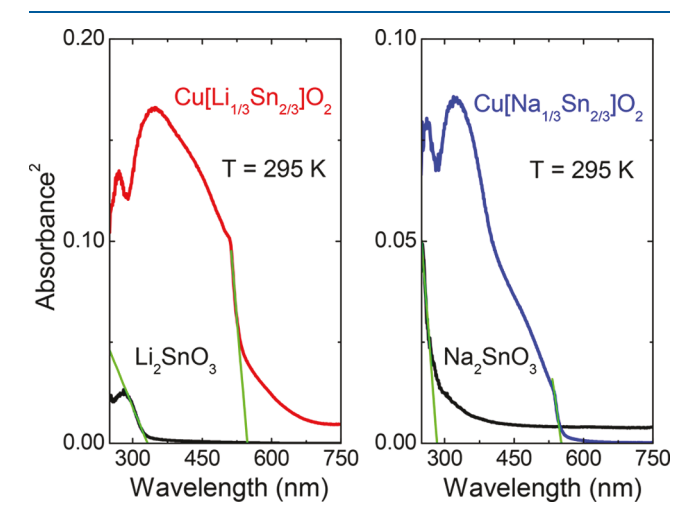


**Figure 2.** Left: Diffuse reflectance spectra plotted as a function of wavelength for Li<sub>2</sub>SnO<sub>3</sub> (= Li[Li<sub>1/3</sub>Sn<sub>2/3</sub>]O<sub>2</sub>) and Cu[Li<sub>1/3</sub>Sn<sub>2/3</sub>]O<sub>2</sub> showing band gap suppression from approximately 4.2 to 2.2 eV. The band gap is estimated from a linear fit to  $\alpha^2$  where  $\alpha$  is the absorption coefficient, assuming a direct band gap. Right: Similar data presented for Na<sub>2</sub>SnO<sub>3</sub> (= Na[Na<sub>1/3</sub>Sn<sub>2/3</sub>]O<sub>2</sub>) and Cu[Na<sub>1/3</sub>Sn<sub>2/3</sub>]O<sub>2</sub> showing a comparable band gap suppression by about 2 eV as a result of copper-exchange reaction. All spectra were collected at room temperature using an integrating sphere in the reflection mode.

reflectance spectra between the parent ternary delafossites and their quaternary derivatives. A substantial red shift is observed in the band gap from approximately 300 nm (4.2 eV) to 550 nm (2.2 eV) as a result of cation exchange. The two-fold reduction of band gap in quaternary delafossites is due to a contribution from Cu 3d electrons to the valence shell. A similar red shift by -1 eV has been reported in related materials  $Ag[Li_{1/3}Sn_{2/3}]O_2$ 

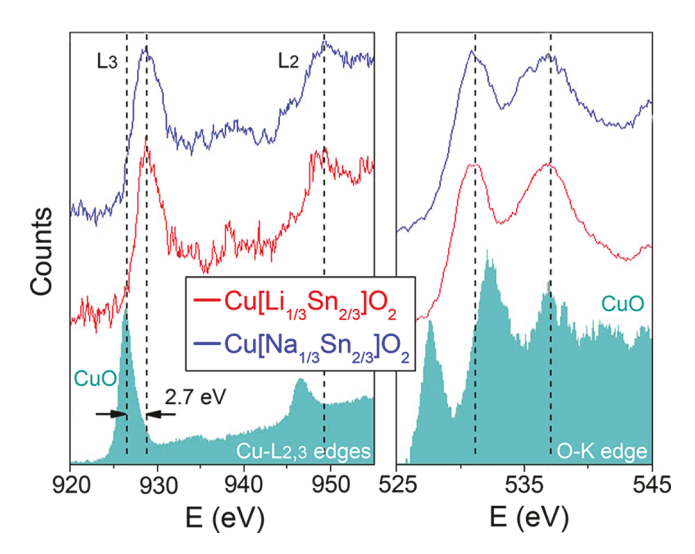


**Figure 3.** EELS data from  $Cu[Li_{1/3}Sn_{2/3}]O_2$  (red) and  $Cu[Na_{1/3}Sn_{2/3}]O_2$  (blue) are compared to a CuO (green) reference. Vertical dashed lines locate the Cu  $L_{2,3}$  and O K edges. The O K edge is identical in both compounds and comparable to the CuO standard as expected. However, both Cu  $L_2$  and  $L_3$  edges are systematically shifted by 2.7 eV between CuO and the title compounds, confirming a  $Cu^+$  oxidation state in the new quaternary delafossites.

and Ag[Li<sub>1/3</sub>Ti<sub>2/3</sub>]O<sub>2</sub> compared to their ternary parent delafossites Li<sub>2</sub>SnO<sub>3</sub> and Li<sub>2</sub>TiO<sub>3</sub> where the contribution from Ag 4d electrons to the valence band is confirmed by X-ray photoelectron spectroscopy (XPS). The effect of copper exchange on the band gap (-2 eV) seems to be even stronger than silver exchange (-1 eV). As a result, copper- or silver-exchanged stannate delafossites are photoactive candidates for sacrificial H<sub>2</sub> evolution from CuCl or AgNO<sub>3</sub> aqueous solutions under visible light.

According to eq 1, we expect copper to stabilize in the oxidation state  $\mathrm{Cu}^+$  after being exchanged with  $\mathrm{Li}^+$  or  $\mathrm{Na}^+$ . This is confirmed in Figure 3 which shows the EELS data from both title compounds and a  $\mathrm{CuO}$  reference. Copper is in the 2+ oxidation state in  $\mathrm{CuO}$  with the  $\mathrm{Cu}\ \mathrm{L_3}$  absorption edge at 926.7 eV. This edge is shifted by 2.7 eV in  $\mathrm{Cu}[\mathrm{Li}_{1/3}\mathrm{Sn}_{2/3}]\mathrm{O}_2$  and  $\mathrm{Cu}[\mathrm{Na}_{1/3}\mathrm{Sn}_{2/3}]\mathrm{O}_2$ , confirming a  $\mathrm{Cu}^+$  oxidation state. The oxygen K edge is identical in both compounds as expected.

**Structural Analysis.** The presence of honeycomb ordering in the monoclinic space group C2/c and its absence in the rhombohedral space group  $R\overline{3}m$ , as visualized in Figure 1a, can be investigated using X-ray diffraction. We performed Rietveld refinements on the PXRD data of Cu[Li<sub>1/3</sub>Sn<sub>2/3</sub>]O<sub>2</sub> and Cu[Na<sub>1/3</sub>Sn<sub>2/3</sub>]O<sub>2</sub> using both rhombohedral and monoclinic models as shown in Figure 4. In the  $R\overline{3}m$  model, each layer is made of edge-sharing  $[A_{1/3}Sn_{2/3}]O_6$  octahedra (A = Li, Na) with ABCABC stacking of layers in a conventional hexagonal unit cell. Adjacent layers are linked by linearly coordinated CuO<sub>2</sub> dumbbells (Cu<sup>+</sup>). The mixed occupancy of in-plane Wyckoff site 3b (A<sub>1/3</sub>Sn<sub>2/3</sub>) corresponds to a lack of honeycomb ordering in this model (see Figure 1a). Figure 4a,b shows the failure of this model to index the broad asymmetric peak between 18° and 21°, although the rest of the peaks are indexed. In the monoclinic C2/c model, the stacking is ABAB (Figure 1b) with adjacent layers linked by CuO2 dumbbells. Importantly, the A/Sn atoms occupy two distinct in-plane Wyckoff sites 4d/8f in this model which corresponds to a honeycomb ordering within the layers (Figure 1a). Figure 4c,d shows the success of this model for indexing all the Bragg peaks including the asymmetric peak in the region 18-21°. The satellite peaks in this region originate from the honeycomb ordering, and their asymmetric broadening, known as Warren line shape, 21 is due to an imperfect stacking of the honeycomb layers. Similar behavior is reported in several ternary and quaternary honeycomb delafossites made

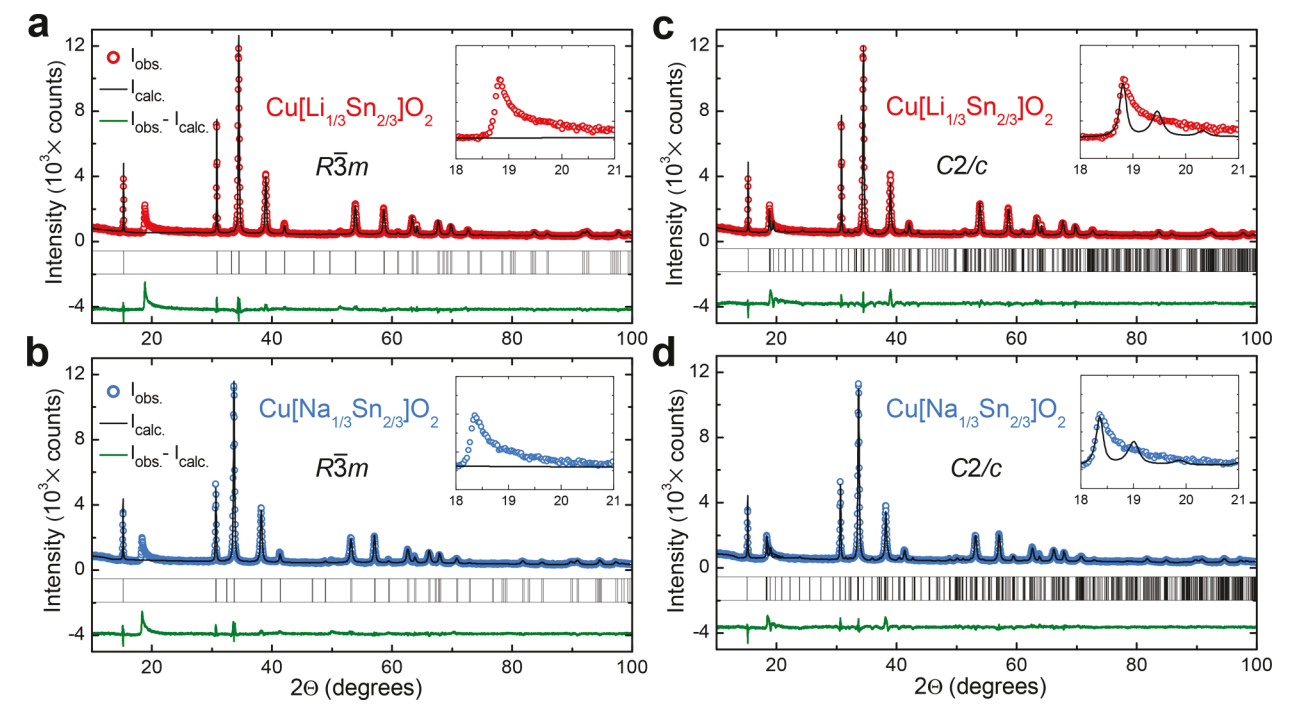


Figure 4. Rietveld refinements of PXRD patterns in the title compounds using  $R\overline{3}m$  and C2/c models. The broad asymmetric peak in the inset is due to the honeycomb ordering which is absent in the rhombohedral model. The monoclinic model allows for honeycomb ordering by placing Sn and the alkali atoms (Li, Na) on distinct Wyckoff sites. A stacking disorder is responsible for the asymmetric broadening of the honeycomb peaks.

Table 1. Crystallographic Data for the Title Compounds, Including Unit Cell Dimensions and Refinement Parameters<sup>a</sup>

$Cu[Li_{1/3}Sn_{2/3}]O_2$	$Cu[Na_{1/3}Sn_{2/3}]O_2$
176.99	182.34
C12/c1	C12/c1
5.4567(1)	5.5938(1)
9.4283(3)	9.6640(4)
11.7486(3)	11.8181(5)
98.975(2)	99.156(2)
597.047	630.738
12	12
5.907	5.761
295	295
12.8	9.07
6.75	6.29
4.17	4.16
6.19	5.60
9.00	7.83
4.67	3.55
	176.99 C12/c1 5.4567(1) 9.4283(3) 11.7486(3) 98.975(2) 597.047 12 5.907 295 12.8 6.75 4.17 6.19 9.00

"Data were obtained at room temperature using Cu–K $\alpha$  radiation with  $\lambda = 1.5406$  Å.  $\chi^2$  values are relatively high due to stacking faults.

of rhodium(IV) and iridium(IV) exchanged with Cu, Ag, or H.  $^{7,12,22,23}$  Tables 1 and 2 summarize the details of our Rietveld refinements. For completeness, we also performed a refinement in the C2/m space group in the Supporting Information (Figure S7). Distinguishing between the C2/m and C2/c space groups is an ongoing challenge in delafossite systems.  $^{12,24-26}$  The C2/m space group offers a simpler model compared to C2/c with a single layer unit cell where the 2b site is fully occupied by Sn and the 4g site is filled with equally mixed A/Sn. Although the fit qualities are acceptable, this model corresponds to an inverse honeycomb ordering where the site with lower multiplicity is occupied by Sn and the site with higher multiplicity by the alkali. This rules out the C2/m model and confirms C2/c as the correct space group.

As mentioned above, adjacent honeycomb layers are linked via O-Cu-O dumbbells (Figure 1b). The small electropositivity and coordination number of Cu<sup>+</sup>, compared to Li<sup>+</sup>/Na<sup>+</sup>, results in a weak interlayer bonding that causes stacking disorders and Warren line shaped peaks on the PXRD patterns in copper-exchanged delafossites. The Warren line shape is

usually assigned to a skipping or shifting of the layers in several quaternary delafossites with bilayer or trilayer stacking. <sup>22,27,28</sup> Here, by performing advanced TEM analysis, we reveal that the Warren line shape in the quaternary stannates is due to a twinning between adjacent layers instead of the conventional skipping or shifting of the layers.

**Transmission Electron Microscopy.** Electron diffraction (ED) is a complementary method to examine the X-ray crystallographic solutions. Figure 5 shows ED patterns from

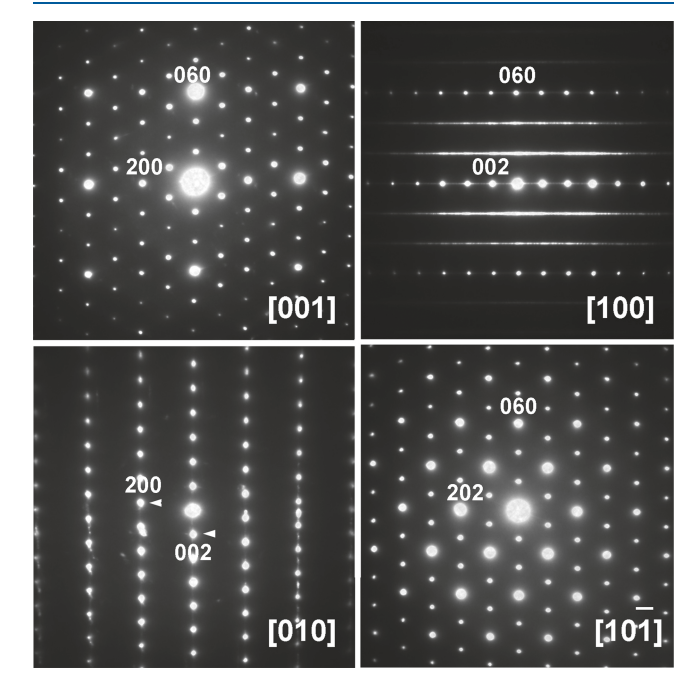


**Figure 5.** ED patterns from  $Cu[Li_{1/3}Sn_{2/3}]O_2$  along four different zone axes are indexed in the monoclonic space group C2/c. The streaking in the [100] diffraction pattern implies a stacking disorder along c-axis.

Cu[Li<sub>1/3</sub>Sn<sub>2/3</sub>]O<sub>2</sub> along four principal crystallographic zone axes including [001], [100], [010], and [10 $\overline{1}$ ]. All diffraction spots are indexed in the space group C2/c in agreement with the X-ray structural solution. Similar results are observed in Cu[Na<sub>1/3</sub>Sn<sub>2/3</sub>]O<sub>2</sub>, confirming a monoclinic unit cell with honeycomb ordering in both quaternary stannates. The streaking in the [100] ED pattern implies some form of stacking disorder,

Table 2. Wyckoff Sites, Atomic Coordinates, and Site Occupancies for the Title Compounds

atom	site	$\text{Cu}[\text{Li}_{1/3}\text{Sn}_{2/3}]\text{O}_2$		$Cu[Na_{1/3}Sn_{2/3}]O_2$				
		$\boldsymbol{x}$	у	z	x	у	z	occupancy
Cu1	4e	0	3/4	1/4	0	3/4	1/4	1.000
Cu2	4e	0	0.4683(6)	1/4	0	0.4703(6)	1/4	1.000
Cu3	4e	0	0.0813(7)	1/4	0	0.0778(8)	1/4	1.000
Sn1	8 <i>f</i>	1/4	0.0760(2)	0	1/4	0.0762(2)	0	0.830(1), 0.854(2)
Li1, Na1	8 <i>f</i>	1/4	0.0760(2)	0	1/4	0.0762(2)	0	0.170(1), 0.146(2)
Sn2	4 <i>d</i>	3/4	1/4	0	3/4	1/4	0	0.339(2), 0.291(4)
Li2, Na2	4 <i>d</i>	3/4	1/4	0	3/4	1/4	0	0.661(2), 0.709(4)
O1	8 <i>f</i>	0.9499	3/4	0.0909	0.9499	3/4	0.0909	1.000
O2	8 <i>f</i>	0.9406	0.4208	0.0781	0.9406	0.4208	0.0781	1.000
O3	8 <i>f</i>	0.9327	0.0848	0.0916	0.9327	0.0848	0.0916	1.000

<sup>&</sup>quot;The isotropic Debye—Waller factors ( $B_{\rm iso}$ ) are less than 1.0 Å<sup>2</sup> for all atoms. Since oxygen atoms are practically invisible to X-rays, their positions are not refined. Instead, oxygen positions are modeled based on the honeycomb structure of  ${\rm Cu_2IrO_3}$ , hence the lack of error in O1, O2, and O3 positions. 7.

reminiscent of the Warren line shape in PXRD. <sup>29–31</sup> As explained above, stacking disorders originate from the weak bonding between the honeycomb layers and could take the form of skipping, shifting, or twinning of the layers. The skipping or shifting of the layers can be observed in high-resolution TEM images as commonly reported in layered oxides. <sup>27,32</sup> In the following, we will show that such stacking faults are absent in  $\text{Cu}[\text{Li}_{1/3}\text{Sn}_{2/3}]\text{O}_2$  and  $\text{Cu}[\text{Na}_{1/3}\text{Sn}_{2/3}]\text{O}_2$ . Instead, a twinning between adjacent layers is the principal form of stacking disorder.

Figure 6 is a HAADF-STEM image from a  $Cu[Li_{1/3}Sn_{2/3}]O_2$  crystallite viewing down the [100] axis, the same direction

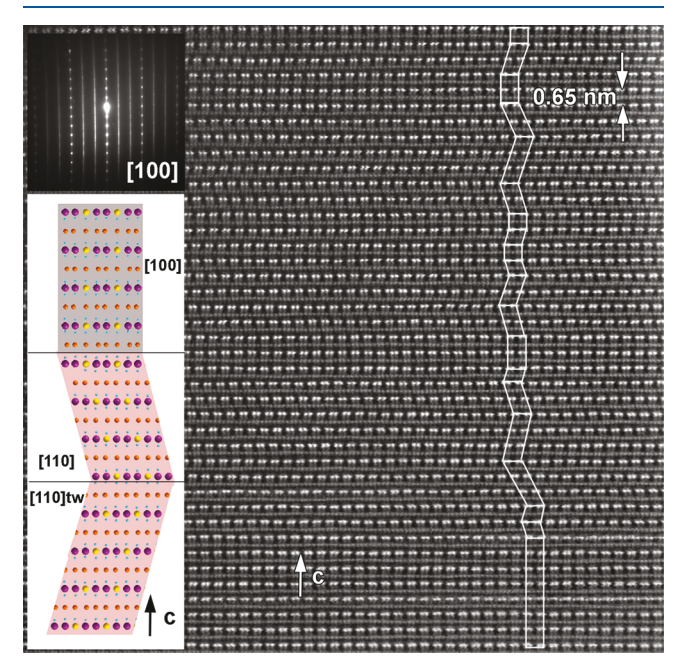


**Figure 6.** HAADF-STEM image of a  $\text{Cu}[\text{Li}_{1/3}\text{Sn}_{2/3}]\text{O}_2$  crystallite with the corresponding ED pattern viewing down the [100] axis. The stacking disorder is modeled as a twinning of the unit cells (inset). The pristine unit cells that are stacked along the *c*-axis form straight columns when viewed down the *a*-axis. Rotational twinning around *c*-axis from [100] to [110]/[110]tw results in left/right inclined stacking.

where streaking is observed in the ED pattern. A characteristic zigzag stacking pattern is observed in the HAADF-STEM image. The bottom nine layers are perfectly stacked along the *c*-axis, forming a straight column of Sn atoms (the brightest dots). The first zigzag occurs between the 10th and the 11th layers corresponding to a twinning from the [100] to [110] zone axis. The twinning results in a left-inclined stacking as modeled in the inset using the X-ray crystallographic solutions. A 60° rotation of the unit cell around the *c*-axis gives rise to a right-inclined stacking and exposes the [110]-twinned zone axis as indicated in the inset.

Figure 7 provides a closer view down the [100] axis in a  $Cu[Na_{1/3}Sn_{2/3}]O_2$  crystallite. The left panel is a HAADF-STEM image, and the right panel is an ABF-STEM image. A characteristic feature in both images is the pairs of tin atoms (highest intensity dots) separated by individual sodium atoms that appear as faint dots due to sodium's small atomic number. This pattern is compelling evidence for the honeycomb ordering within each  $[Na_{1/3}Sn_{2/3}]$  layer where the 2/1 ratio of Sn/Na is constrained by the multiplicity of their distinct 8f/4d Wyckoff sites in the C2/c space group, as explained in the

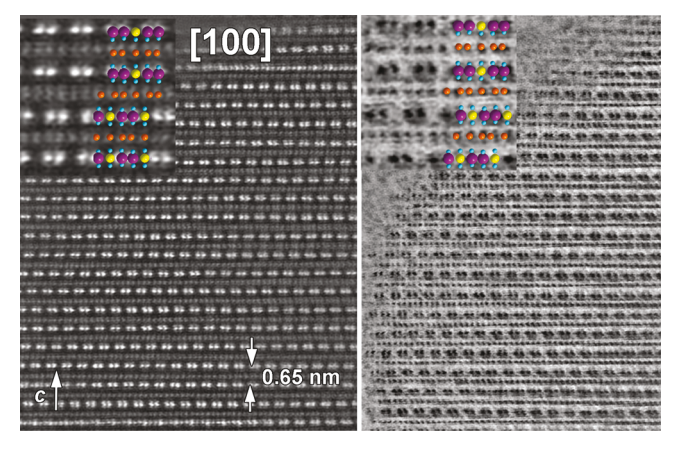
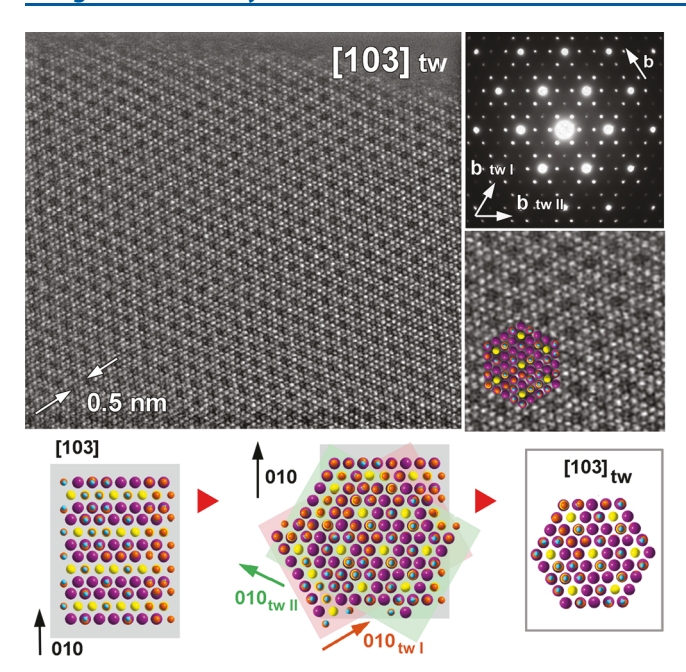


Figure 7. HAADF-STEM (left) and ABF-STEM (right) images of a  $\text{Cu}[\text{Na}_{1/3}\text{Sn}_{2/3}]\text{O}_2$  crystallite projected down the [100] zone axis. The brightest dots in the dark-field image (left) are tin atoms (Z=50), and the less bright dots are copper atoms (Z=29). Each pair of tin atoms (highest intensity dots) are separated by one sodium atom (faint intensity due to small atomic number Z=11) in both images. This is a direct result of honeycomb ordering in each layer as explained in the text. Tin, copper, oxygen, and alkali atoms are modeled as purple, orange, blue, and yellow circles. In the bright-field image (right), the oxygen atoms (pale gray dots) in each layer organize so that they form a linear coordination with the copper atoms between the layers.

Introduction (Figure 1). Copper atoms appear as smaller dots between the  $[\mathrm{Na_{1/3}Sn_{2/3}}]\mathrm{O_6}$  honeycomb layers in both the dark-field and bright-field images. The ABF-STEM image in Figure 7 shows the presence of oxygen atoms (modeled as small blue circles) on top and bottom of each copper atom (orange circles) forming  $\mathrm{CuO_2}$  dumbbells. Oxygen deficiency is a common source of skipping layers. Our modeling of the copper and oxygen atoms in Figure 7 rules out the oxygen deficiency and skipping or shifting of the layers.

Figure 8 provides a direct view over the honeycomb layers with a projection along the [103] axis in  $\text{Cu}[\text{Li}_{1/3}\text{Sn}_{2/3}]\text{O}_2$ . At first glance, the pattern seems hexagonal instead of honeycomb in the HAADF-STEM image. However, this pattern is accurately modeled as a twinned stacking of honeycomb layers. In the model, the first layer at the bottom has the *b*-axis pointing forward, the second layer is rotated clockwise by +60°, and the third layer is rotated anticlockwise by -60° (Figure 8, bottom). As a result, the alkali atoms (modeled as yellow circles) stack on top of each other and produce a hexagonal pattern. This is confirmed by the ED pattern in the inset of Figure 8 where the Bragg spots are fully indexed by two twinned *b*-axes.

Heat Capacity. Both  $Cu[Li_{1/3}Sn_{2/3}]O_2$  and  $Cu[Na_{1/3}Sn_{2/3}]O_2$  are nonmagnetic insulating materials, so their heat capacity originates entirely from phonons without contributions from electrons or magnons (Figure S8). For the determined crystal structures, we used the TDEP approach  $^{16,17}$  to calculate the lattice heat capacities. In this approach, thermally relevant configurations of displaced atoms, including their zero-point motion, are generated within a supercell. The corresponding forces on each atom are calculated using density functional theory from which interatomic force constants (the unknowns that relate the displacements to the forces) are then determined. The dynamical matrix is diagonalized to obtain phonon modes, from which the lattice heat capacities are calculated. Calculations are performed on both the parent ternary delafossites and the new quaternary systems made here by



**Figure 8.** HAADF-STEM image projected down the [103] axis to reveal the honeycomb layers in  $Cu[Li_{1/3}Sn_{2/3}]O_2$ . The corresponding ED pattern and a magnified view with overlaid model are given in the inset. At first, the pattern seems to be hexagonal instead of honeycomb. However, taking into account the twinning observed in the [100] zone (Figure 6), this pattern is modeled as a stacking of honeycomb layers with two twinned b-axes as shown in the bottom inset.

copper exchange. The results are presented in Figure 9 and compared to the experimental measurements. Figure 9a shows the experimental heat capacity as a function of temperature for the ternary delafossite  $Na[Na_{1/3}Sn_{2/3}]O_2$  (orange circles) and

the copper-exchanged system Cu[Na<sub>1/3</sub>Sn<sub>2/3</sub>]O<sub>2</sub> (blue circles). Solid lines represent the calculated heat capacity for each compound. A remarkable agreement is observed between the experimental data and the calculated C(T) curves. Figure 9b,c shows the phonon density of states (DOS) in Na[Na<sub>1/3</sub>Sn<sub>2/3</sub>]- $O_2$  and  $Cu[Na_{1/3}Sn_{2/3}]O_2$  where the partial contribution from Cu, Na, Sn, and O appears as light orange, dark orange, light green, and dark green. Several peaks and troughs are observed in the DOS with increasing frequency equivalent to increasing temperature (1 THz  $\approx$  50 K). Figure 9b shows that the main contribution to the DOS in Na[Na<sub>1/3</sub>Sn<sub>2/3</sub>]O<sub>2</sub> at low frequencies is from the SnO<sub>6</sub> octahedra and the contribution from Na is not significant below 3 THz. Figure 9c shows that both CuO2 dumbbells and SnO6 octahedra contribute to the lowenergy heat capacity of Cu[Na<sub>1/3</sub>Sn<sub>2/3</sub>]O<sub>2</sub> below 3 THz. This is related to the heavier mass of Cu compared to Na that makes phonons acoustic branches less dispersive and produces a large DOS (dispersion curves are presented in Figure S9 in the Supporting Information). A larger DOS at lower frequencies (f < 3 THz) produces a higher heat capacity at lower temperatures (T < 150 K) in  $Cu[Na_{1/3}Sn_{2/3}]O_2$  compared to Na[Na<sub>1/3</sub>Sn<sub>2/3</sub>]O<sub>2</sub>. There is a deep trough in the DOS of Cu[Na<sub>1/3</sub>Sn<sub>2/3</sub>]O<sub>2</sub> at approximately 3 THz corresponding to 150 K. In contrast, Na[Na<sub>1/3</sub>Sn<sub>2/3</sub>]O<sub>2</sub> shows a smoother variation of DOS across 3 THz. As a result, a crossing occurs between the heat capacity curves of  $Na[Na_{1/3}Sn_{2/3}]O_2$  and Cu[Na<sub>1/3</sub>Sn<sub>2/3</sub>]O<sub>2</sub> at approximately 150 K. The crossing temperature from calculations is in excellent agreement with the experimental observation in Figure 9a.

Figure 9d–f shows the results of our calculations for  $Li[Li_{1/3}Sn_{2/3}]O_2$  (green circles) and  $Cu[Li_{1/3}Sn_{2/3}]O_2$  (red circles). Similar to the sodium compounds, copper exchange results in an enhanced DOS and a higher heat capacity at low

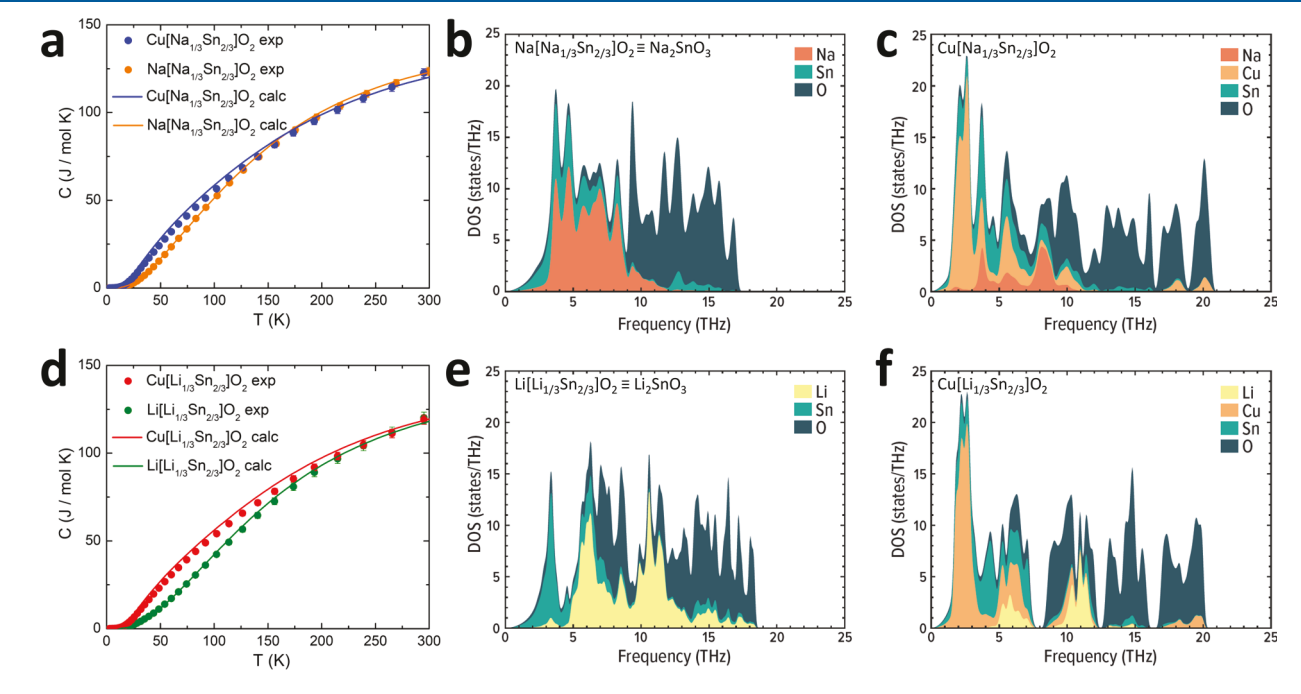


Figure 9. (a) Heat capacity plotted as a function of temperature for  $Cu[Na_{1/3}Sn_{2/3}]O_2$  (blue) and  $Na[Na_{1/3}Sn_{2/3}]O_2$  (orange) from experiments and calculations. A crossing between the measured heat capacity of the two compounds is observed at approximately 150 K which is reproduced by the calculations. (b) Partial phonon density of states (DOS) from Na, Sn, and O plotted as a function of frequency in  $Na[Na_{1/3}Sn_{2/3}]O_2$ . (c) Partial phonon DOS from Na, Cu, Sn, and O in  $Cu[Na_{1/3}Sn_{2/3}]O_2$ . (d) Heat capacity plotted as a function of temperature for  $Cu[Li_{1/3}Sn_{2/3}]O_2$  (red) and  $Li[Li_{1/3}Sn_{2/3}]O_2$  (green). (e) Partial phonon DOS from Li, Sn, and O plotted as a function of frequency in  $Li[Li_{1/3}Sn_{2/3}]O_2$ . (f) Partial phonon DOS from Li, Cu, Sn, and O in  $Cu[Li_{1/3}Sn_{2/3}]O_2$ .

temperatures (T < 150 K and f < 3 THz) due to the heavier mass of Cu compared to Li. The difference in DOS and the separation between the two heat capacity curves before and after the copper exchange is more prominent in the lithium compounds (Figure 9d-f) compared to the sodium compounds (Figure 9a-c) because lithium atoms are three times lighter than sodium atoms. Unlike the sodium compounds, both the ternary Li[Li<sub>1/3</sub>Sn<sub>2/3</sub>]O<sub>2</sub> and the quaternary Cu-[Li<sub>1/3</sub>Sn<sub>2/3</sub>]O<sub>2</sub> exhibit a deep trough in their DOS at approximately 4 THz. Therefore, the two calculated heat capacity curves in Figure 9d smoothly merge near room temperature without crossing, in perfect agreement with the experimental data. Note that we did not include defects in our computations. In principle, the effect of stacking disorder could be included in the TDEP calculations by using a large supercell, but this is computationally too expensive and inaccessible. Furthermore, we do not expect the twinned stacking faults to affect phonon dispersions because the twinning between the layers corresponds to a rigid rotation of O-Cu-O bonds without changing the bond strength or the bond angles. A rigid angular translation will not cost energy and will not affect the phonon modes. However, bond angles will be affected in materials with missing or shifting of the layers, but such stacking faults are absent in the stannates presented here.

#### CONCLUSIONS

Topotactic cation-exchange reaction is a versatile technique to fabricate a variety of new layered magnetic and thermoelectric materials. We specifically targeted two nonmagnetic and insulating quaternary delafossites with honeycomb ordering to establish a reliable method of analyzing the lattice heat capacity in such materials. Our detailed structural and chemical analyses show that Cu<sup>+</sup> is stabilized in a dumbbell O-Cu-O coordination between the honeycomb layers in both title compounds. Our TEM analysis uncovers a stacking disorder in the form of twinning between adjacent layers without skipping or shifting of the layers. We calculate the heat capacity of these complex oxides using a TDEP approach and demonstrate a remarkable agreement with the experimental data. The analysis presented here for nonmagnetic ternary and quaternary delafossites gives a high level of confidence to our theoretical methods and paves the way to reliably calculate the phonon contribution to the heat capacity of the magnetic delafossite materials.

# ASSOCIATED CONTENT

# **S** Supporting Information

The Supporting Information is available free of charge on the ACS Publications website at DOI: 10.1021/acs.inorgchem.8b01866.

Controlling the stacking disorder in  $Na_2SnO_3$ , thermal analysis, effect of the ionic size on the exchange reaction, energy-dispersive X-ray spectroscopy, inductively coupled plasma optical emission spectroscopy, Reitveld refinement in C2/m space group, residual linear term in heat capacity, phonon dispersions (PDF)

# **Accession Codes**

CCDC 1855314 and 1855315 contain the supplementary crystallographic data for this paper. These data can be obtained free of charge via www.ccdc.cam.ac.uk/data\_request/cif, or by emailing data\_request@ccdc.cam.ac.uk, or by contacting The Cambridge Crystallographic Data Centre, 12 Union Road, Cambridge CB2 1EZ, UK; fax: +44 1223 336033.

## AUTHOR INFORMATION

# **Corresponding Author**

\*E-mail: fazel.tafti@bc.edu. Phone: (617) 552-2127.

#### ORCID

Fazel Tafti: 0000-0002-5723-4604

#### Notes

The authors declare no competing financial interest.

#### ACKNOWLEDGMENTS

F.T. and M.A. acknowledge support from the National Science Foundation, Award No. DMR-1708929. D.B. and O.H. acknowledge support from the EFRI-2DARE program of the National Science Foundation, Award No. 1433467. The authors would like to mention the financial support from the "Agence Nationale de la Recherche" in the framework of the "Investissements d'avenir" program with the reference "ANR-11-EQPX-0020" for EELS data obtained using GIF Quantum.

#### REFERENCES

- (1) Shannon, R. D.; Rogers, D. B.; Prewitt, C. T. Chemistry of noble metal oxides. I. Syntheses and properties of ABO<sub>2</sub> delafossite compounds. *Inorg. Chem.* **1971**, *10*, 713–718.
- (2) Smaha, R. W.; Roudebush, J. H.; Herb, J. T.; Seibel, E. M.; Krizan, J. W.; Fox, G. M.; Huang, Q.; Arnold, C. B.; Cava, R. J. Tuning Sodium Ion Conductivity in the Layered Honeycomb Oxide Na<sub>3-x</sub>Sn<sub>2x</sub>Sb<sub>x</sub>NaO<sub>6</sub>. *Inorg. Chem.* **2015**, *54*, 7985–7991.
- (3) Ramesha, K.; Prakash, A. S.; Sathiya, M.; Madras, G.; Shukla, A. K. Synthesis and photocatalytic properties of Ag[Li<sub>1/3</sub>Ru<sub>2/3</sub>]O<sub>2</sub>: A new delafossite oxide. *Mater. Sci. Eng., B* **2011**, *176*, 141–146.
- (4) Gu, J.; Yan, Y.; Krizan, J. W.; Gibson, Q. D.; Detweiler, Z. M.; Cava, R. J.; Bocarsly, A. B. p-Type CuRhO<sub>2</sub> as a Self-Healing Photoelectrode for Water Reduction under Visible Light. *J. Am. Chem. Soc.* **2014**, *136*, 830–833.
- (5) Koumoto, K.; Koduka, H.; Seo, W.-S. Thermoelectric properties of single crystal CuAlO<sub>2</sub> with a layered structure. *J. Mater. Chem.* **2001**, *11*, 251–252.
- (6) Chun, S. H.; et al. Direct evidence for dominant bond-directional interactions in a honeycomb lattice iridate Na<sub>2</sub>IrO<sub>3</sub>. *Nat. Phys.* **2015**, 11, 462–466.
- (7) Abramchuk, M.; Ozsoy-Keskinbora, C.; Krizan, J. W.; Metz, K. R.; Bell, D. C.; Tafti, F. Cu<sub>2</sub>IrO<sub>3</sub>: A New Magnetically Frustrated Honeycomb Iridate. *J. Am. Chem. Soc.* **2017**, *139*, 15371–15376.
- (8) Kitaev, A. Anyons in an exactly solved model and beyond. *Ann. Phys.* **2006**, 321, 2–111.
- (9) Jackeli, G.; Khaliullin, G. Mott Insulators in the Strong Spin-Orbit Coupling Limit: From Heisenberg to a Quantum Compass and Kitaev Models. *Phys. Rev. Lett.* **2009**, *102*, 017205.
- (10) Singh, Y.; Gegenwart, P. Antiferromagnetic Mott insulating state in single crystals of the honeycomb lattice material Na<sub>2</sub>IrO<sub>3</sub>. *Phys. Rev. B: Condens. Matter Mater. Phys.* **2010**, 82, 064412.
- (11) Mehlawat, K.; Thamizhavel, A.; Singh, Y. Heat capacity evidence for proximity to the Kitaev quantum spin liquid in  $A_2IrO_3$  A = (Na, Li). *Phys. Rev. B: Condens. Matter Mater. Phys.* **2017**, 95, 144406.
- (12) Roudebush, J. H.; Ross, K. A.; Cava, R. J. Iridium containing honeycomb Delafossites by topotactic cation exchange. *Dalton Trans* **2016**, *45*, 8783–8789.
- (13) Rodríguez-Carvajal, J. Recent advances in magnetic structure determination by neutron powder diffraction. *Phys. B* **1993**, *192*, 55–69.
- (14) Salter, C. Error Analysis Using the Variance-Covariance Matrix. *J. Chem. Educ.* **2000**, *77*, 1239.
- (15) Jacquez, J. A.; Kuppenheim, H. F. Theory of the Integrating Sphere. J. Opt. Soc. Am. 1955, 45, 460–470.

(16) Hellman, O.; Abrikosov, I. A.; Simak, S. I. Lattice dynamics of anharmonic solids from first principles. *Phys. Rev. B: Condens. Matter Mater. Phys.* **2011**, *84*, 180301.

- (17) Hellman, O.; Steneteg, P.; Abrikosov, I. A.; Simak, S. I. Temperature dependent effective potential method for accurate free energy calculations of solids. *Phys. Rev. B: Condens. Matter Mater. Phys.* **2013**, 87, 104111.
- (18) Kresse, G.; Furthmüller, J. Efficient iterative schemes for ab initio total-energy calculations using a plane-wave basis set. *Phys. Rev. B: Condens. Matter Mater. Phys.* **1996**, *54*, 11169.
- (19) Hosogi, Y.; Kato, H.; Kudo, A. Visible light response of  $AgLi_{1/3}M_{2/3}O_2$  (M = Ti and Sn) synthesized from layered  $Li_2MO_3$  using molten  $AgNO_3$ . *J. Mater. Chem.* **2008**, *18*, 647–653.
- (20) Wang, Y.; Lany, S.; Ghanbaja, J.; Fagot-Revurat, Y.; Chen, Y. P.; Soldera, F.; Horwat, D.; Mucklich, F.; Pierson, J. F. Electronic structures of Cu<sub>2</sub>O, Cu<sub>4</sub>O<sub>3</sub>, and CuO: A joint experimental and theoretical study. *Phys. Rev. B: Condens. Matter Mater. Phys.* **2016**, *94*, 245418.
- (21) Balzar, D. X-Ray Diffraction Line Broadening: Modeling and Applications to High-T<sub>c</sub> Superconductors. *J. Res. Natl. Inst. Stand. Technol.* **1993**, 98, 321–353.
- (22) Todorova, V.; Leineweber, A.; Kienle, L.; Duppel, V.; Jansen, M. On AgRhO<sub>2</sub>, and the new quaternary delafossites AgLi<sub>1/3</sub>M<sub>2/3</sub>O<sub>2</sub>, syntheses and analyses of real structures. *J. Solid State Chem.* **2011**, 184, 1112–1119.
- (23) Bette, S.; Takayama, T.; Kitagawa, K.; Takano, R.; Takagi, H.; Dinnebier, R. E. Solution of the heavily stacking faulted crystal structure of the honeycomb iridate H<sub>3</sub>LiIr<sub>2</sub>O<sub>6</sub>. *Dalton Trans* **2017**, *46*, 15216–15227.
- (24) Krizan, J. W.; Roudebush, J. H.; Fox, G. M.; Cava, R. J. The chemical instability of  $Na_2IrO_3$  in air. *Mater. Res. Bull.* **2014**, *52*, 162–166.
- (25) Politaev, V. V.; Nalbandyan, V. B.; Petrenko, A. A.; Shukaev, I. L.; Volotchaev, V. A.; Medvedev, B. S. Mixed oxides of sodium, antimony (5+) and divalent metals (Ni, Co, Zn or Mg). *J. Solid State Chem.* **2010**, *183*, 684–691.
- (26) Zvereva, E. A.; Stratan, M. I.; Ushakov, A. V.; Nalbandyan, V. B.; Shukaev, I. L.; Silhanek, A. V.; Abdel-Hafiez, M.; Streltsov, S. V.; Vasiliev, A. N. Orbitally induced hierarchy of exchange interactions in the zigzag antiferromagnetic state of honeycomb silver delafossite Ag<sub>3</sub>Co<sub>2</sub>SbO<sub>6</sub>. Dalton Trans 2016, 45, 7373–7384.
- (27) Roudebush, J. H.; Andersen, N. H.; Ramlau, R.; Garlea, V. O.; Toft-Petersen, R.; Norby, P.; Schneider, R.; Hay, J. N.; Cava, R. J. Structure and Magnetic Properties of Cu<sub>3</sub>Ni<sub>2</sub>SbO<sub>6</sub> and Cu<sub>3</sub>Co<sub>2</sub>SbO<sub>6</sub> Delafossites with Honeycomb Lattices. *Inorg. Chem.* **2013**, *52*, 6083–6095.
- (28) Wallace, D. C.; Brown, C. M.; McQueen, T. M. Evolution of magnetism in the  $Na_{3-\delta}(Na_{1-x}Mg_x)Ir_2O_6$  series of honeycomb iridates. *J. Solid State Chem.* **2015**, 224, 28–35.
- (29) Zhao, H.; Qiu, B.; Guo, H.; Jia, K.; Liu, Z.; Xia, Y. Characterization of Li-rich layered oxides by using transmission electron microscope. *Green Energy & Environment* **2017**, *2*, 174–185.
- (30) Mortemard de Boisse, B.; Liu, G.; Ma, J.; Nishimura, S.-i.; Chung, S.-C.; Kiuchi, H.; Harada, Y.; Kikkawa, J.; Kobayashi, Y.; Okubo, M.; Yamada, A. Intermediate honeycomb ordering to trigger oxygen redox chemistry in layered battery electrode. *Nat. Commun.* **2016**, *7*, 11397.
- (31) Zaikina, J. V.; Kovnir, K. A.; Sobolev, A. N.; Presniakov, I. A.; Kytin, V. G.; Kulbachinskii, V. A.; Olenev, A. V.; Lebedev, O. I.; Van Tendeloo, G.; Dikarev, E. V.; Shevelkov, A. V. Highly Disordered Crystal Structure and Thermoelectric Properties of Sn<sub>3</sub>P<sub>4</sub>. *Chem. Mater.* **2008**, *20*, 2476–2483.
- (32) Talantsev, E. F.; Wimbush, S. C.; Strickland, N. M.; Xia, J. A.; D'Souza, P.; Storey, J. G.; Tallon, J. L.; Ingham, B.; Knibbe, R.; Long, N. J. Oxygen Deficiency, Stacking Faults and Calcium Substitution in MOD YBCO Coated Conductors. *IEEE Trans. Appl. Supercond.* 2013, 23, 7200205.
- (33) Sun, Y.; Cong, H.; Zan, L.; Zhang, Y. Oxygen Vacancies and Stacking Faults Introduced by Low-Temperature Reduction Improve

the Electrochemical Properties of Li<sub>2</sub>MnO<sub>3</sub> Nanobelts as Lithium-Ion Battery Cathodes. ACS Appl. Mater. Interfaces **2017**, *9*, 38545–38555.